Atmos. Meas. Tech. Discuss., 4, 7657–7698, 2011
www.atmos-meas-tech-discuss.net/4/7657/2011/
doi:10.5194/amtd-4-7657-2011

Atmospheric Measurement Techniques Discussions

Satellite retrieval of the liquid water fraction in tropical clouds between −20 and −38 °C

D. L. Mitchell[1] **and R. P. d'Entremont**[2]

[1]Desert Research Institute, 2215 Raggio Parkway, Reno, Nevada, 89512-1095, USA
[2]Atmospheric and Environmental Research, Inc., 131 Hartwell Ave., Lexington, Massachusetts, 02421-3126, USA

Received: 8 November 2011 – Accepted: 30 November 2011 – Published: 20 December 2011

Correspondence to: D. L. Mitchell (david.mitchell@dri.edu)

Published by Copernicus Publications on behalf of the European Geosciences Union.

Abstract

This study describes a satellite remote sensing method for directly retrieving the liquid water fraction in mixed phase clouds, and appears unique in this respect. The method uses MODIS split-window channels for retrieving the liquid fraction from cold clouds where the liquid water fraction is less than 50 % of the total condensate. This makes use of the observation that clouds only containing ice exhibit effective 12-to-11 μm absorption optical thickness ratios (β_{eff}) that are quasi-constant with retrieved cloud temperature T. This observation was made possible by using two CO_2 channels to retrieve T and then using the 12 and 11 μm channels to retrieve emissivities and β_{eff}. Thus for $T < -40\,^{\circ}\text{C}$, β_{eff} is constant, but for $T > -40\,^{\circ}\text{C}$, β_{eff} slowly increases due to the presence of liquid water, revealing mean liquid fractions of ~10 % around $-22\,^{\circ}\text{C}$ from tropical clouds identified as cirrus by the cloud mask. However, the uncertainties for these retrievals are large, and extensive in situ measurements are needed to refine and validate these retrievals. Such liquid levels are shown to reduce the cloud effective diameter D_{e} such that cloud optical thickness will increase by more than 50 % for a given water path, relative to D_{e} corresponding to pure ice clouds. Such retrieval information is needed for validation of the cloud microphysics in climate models. Since low levels of liquid water can dominate cloud optical properties, tropical clouds between −25 and $-20\,^{\circ}\text{C}$ may be susceptible to the first aerosol indirect effect.

1 Introduction

While much attention has been paid to boundary layer clouds and cirrus clouds, relatively little research has been conducted on midlevel nonprecipitating clouds, even though altocumulus and altostratus clouds cover 22 % of the Earth's surface (Warren et al., 1988). Matveev (1984) found that more than 30 % of the clouds between −8 and $-26\,^{\circ}\text{C}$ were mixed phase. In a detailed field study of mixed phase clouds associated with frontal systems (Korolev et al., 2003), such clouds tended to be predominantly

AMTD
4, 7657–7698, 2011

liquid or ice, rarely having comparable fractions of ice and liquid. Comparisons with other field studies revealed that the ice fraction (relative to the total water content) varies widely for a given temperature.

Many studies have failed to find a relationship between cloud phase and temperature (Hobbs and Rangno, 1985; Heymsfield et al., 1991; Lawson et al., 2001; Pinto et al., 2001; Fleishauer et al., 2002; Korolev et al., 2003). Hobbs and Rangno (1998) found that cloud phase was most related to cloud age.

Progress has been made in recent years regarding the ground-based remote sensing of mixed phase clouds, especially in the Arctic where clouds are often mixed phase (Curry et al., 1996). For example, an Arctic mixed phase cloud algorithm has been developed for distinguishing cloud radar Doppler spectra into liquid and ice components (Shupe et al., 2004). Optically thin (visible optical thickness < 6) single layer Arctic mixed phase clouds have been characterized in terms of their optical thickness, their ice water fraction, and the effective diameter for water and ice particles using high-resolution infrared radiance and lidar cloud boundary observations (Turner et al., 2005). Still needed are retrievals that can simultaneously characterize the water phase, liquid water content (LWC) and ice water content (IWC), and the effective particle size D_e for water and ice at all altitudes.

Recent progress has also been made regarding the satellite remote sensing of mixed-phase clouds, due primarily to the A-train satellite constellation containing the CALIPSO (Cloud-Aerosol Lidar Pathfinder Satellite Observations) satellite with its CALIOP (Cloud-Aerosol Lidar with Orthogonal Polarization) lidar that measures the depolarization of the cloud elements. The depolarization ratio is used to estimate the thermodynamic phase of the cloud particles. Satellite remote sensing studies have detected liquid water between -20 and $-36\,^{\circ}$C at all latitudes (Yoshida et al., 2010; Hu et al., 2010), compiling global statistics on the frequency of occurrence of these mixed-phase clouds, as well as the temperature dependence of their liquid water content and path. However, these studies did not retrieve an estimate of the mean liquid water fraction in a cloud field, which is the goal of this study. This combined knowledge

AMTD
4, 7657–7698, 2011

should be very helpful for improving cloud-climate feedbacks in global climate models (Hu et al., 2010; Li and Le Treut, 1992).

In general, the liquid fraction in Arctic mixed phase clouds exceeds 40 % (Zhao and Wang, 2010). Due to the relatively high projected area of cloud water droplets relative to ice crystals (per unit mass) and the noted liquid fraction, the liquid phase governs the optical properties of Arctic mixed phase clouds (Shupe and Intrieri, 2004). Thus the ice phase in these clouds bears significance to the cloud life cycle (i.e. relatively high fall speeds of ice particles accelerate the removal of condensate from the cloud) but it has a relatively weak impact on the cloud optical properties.

A different situation may exist for cold clouds containing low levels of liquid water. In this case the presence of liquid may have little effect on the cloud life cycle but it would have a large impact on the cloud optical properties. This is because a small increase in the cloud liquid fraction results in a large increase in the projected area of the size distribution of water and ice particles, provided the liquid fraction is small relative to the total condensate.

This study describes a satellite remote sensing method for retrieving the liquid water fraction from cold clouds ($\lesssim -20\,^{\circ}$C) where the liquid fraction is below 50 %. Low levels of liquid coexisting with ice (or predominately liquid clouds coexisting with ice clouds) need to be quantified in order to realistically describe the radiative properties of these clouds. This paper is organized by presenting the cloud temperature/emissivity retrieval methodology in Sect. 2, followed by a description of the liquid fraction retrieval concept in Sect. 3. After describing the microphysics retrieval algorithm in Sect. 4, results and an uncertainty analysis are presented in Sect. 5. The dependence of cloud optics on the retrieved liquid water fraction is given in Sect. 6, and a summary is given in Sect. 7.

2 Satellite observations of the absorption optical thickness ratio

For cirrus clouds over ocean the approach we take here to retrieve emissivity is first to use the 13.3 and 14.2-μm carbon-dioxide channels of the Moderate Resolution Imaging

AMTD
4, 7657–7698, 2011

Spectroradiometer (MODIS) to retrieve cloud effective temperature. Once the cloud temperature is retrieved, we exploit the thermal-infrared (TIR) window channels at 11 and 12 μm to obtain the cloud emissivities. This method is outlined as follows.

The satellite-observed infrared upwelling radiance I_{TOA} for a non-scattering atmosphere in local thermodynamic equilibrium is expressed as:

$$I_{TOA} = \varepsilon_{SFC} B(\lambda, T_{SFC}) \tau_{ATM} + \int_{\tau_{ATM}} B(\lambda, T) d\tau + (1 - \varepsilon_{SFC}) \tau_{ATM} \int_{\tau^*_{ATM}} B(\lambda, T) d\tau^* , \quad (1)$$

where ε_{SFC} is the TIR surface emissivity, B is the Planck function, λ is wavelength, τ is the upward atmospheric transmittance profile (from top of atmosphere (TOA) down to some level), and τ^* is the downward transmittance (from the surface up to some level). Atmospheric transmittance for the path between TOA and the Earth's surface is denoted by τ_{ATM}. In general $\tau \neq \tau^*$, but note that $\tau_{ATM} = \tau^*_{ATM}$ since the path from space to the surface and vice versa is the same, regardless of direction. The first term on the right side of this equation denotes the contribution to the satellite observed radiance from the Earth's surface. The second term is the upwelling surface energy that is absorbed by the atmosphere and re-emitted to space at its own temperature. The third term represents downwelling atmospheric energy that is reflected to space by the Earth's surface.

For the clear atmosphere over ocean surfaces we prescribe all of the terms in Eq. (1) for a given satellite pixel with coincident numerical weather predicition (NWP) atmospheric profiles of pressure, temperature and water vapor (for τ and $T(\tau)$); a sea-surface temperature analysis (for T_{SFC}); and the ocean-surface emissivity model of Nalli et al. (2008) for ε_{SFC}. We gather the NWP profiles from the Global Forecast System (GFS) maintained by the National Centers for Environmental Predicition (NCEP). The atmospheric optical thicknesses $\delta(s)$ and transmittances $\tau = e^{\int \delta(s) ds}$ are computed for any given path "*ds*" using the Optimal Spectral Sampling (OSS) model of Moncet et al. (2004).

AMTD
4, 7657–7698, 2011

Now when a "flat-slab" or single-layer cirrus cloud (common in the retrieval literature: see, for example, Inoue, 1985; Parol et al., 1991) is introduced into the pixel, the atmospheric optical thickness $\delta_{TOT} = \delta_{ATM} + \delta_{CLD}$ contains both a clear and a cloudy component at the cloud level. Therefore once the cloud physical temperature and absorption optical thickness are prescribed it is possible to re-estimate the upwelling infrared radiance using Eq. (1) for cirrus conditions by adjusting the clear-atmosphere optical thickness – and subsequently the corresponding transmittance profile – for the cloudy condition.

The next logical step is to select as the cirrus retrieval those thermodynamic (temperature) and radiative (absorption optical thickness) properties that yield simultaneously the best match among satellite-observed radiances and those predicted by Eq. (1). Typically the cirrus retrieval problem is posed in terms of at least these two unknowns: cloud temperature and absorption optical thickness. Thus Eq. (1) requires two cloud variables to compute one cloudy radiance, implying that the retrieval problem must somehow be constrained since there are two unkowns and only one known. At this point a second radiance can be introduced, seemingly matching now the number of unknown and known variables. However the introduction of a new wavelength brings in another variable in the form of a new wavelength-dependent optical thickness, leaving three unknowns and only two knowns.

The conventional approach out of this conundrum is to find a relationship between the cirrus emissivities across these two wavelengths to obtain closure from a mathematical viewpoint (Inoue, 1985; Parol et al., 1991; Giraud et al., 1997). This does not serve our purposes well, however, since we must retrieve 11 and 12-μm cloud emissivities that have no such constraint inherently built into them if we intend to extract microphysical attributes from them with no pre-determined bias.

2.1 Solving for cloud temperature and emissivity

Cirrus cloud temperature is estimated using radiances measured in two of the MODIS carbon dioxide channels at 13.3 and 14.2 μm, respectively referred to as channels

AMTD
4, 7657–7698, 2011

A and B. For ice clouds, the real refractive index, n_r, at 13.3 and 14.2 µm is 1.52 and 1.58, respectively, indicating the absorption contribution from photon tunneling (i.e. wave resonance) is almost the same in these channels (Mitchell, 2000; Mitchell et al., 2010). The imaginary index n_i is 0.355 and 0.246, respectively, generally yielding an ice particle size distribution (PSD) absorption efficiency $Q_{abs} \approx 1.0$ for each wavelength when tunneling is neglected (Mitchell et al., 2010). That is, all radiation incident on the particle cross-section is absorbed. This means that the combined effects of tunneling and Beer's Law absorption render approximately equal absorption optical thickness in each channel for a given PSD or effective diameter D_e. This is shown by the solid curves in Fig. 1, where Q_{abs} for these two CO_2 absorption channels are plotted as a function of D_e (as defined in Mitchell, 2002). Note that $Q_{abs} = \beta_{abs}/A_{PSD}$, where β_{abs} is the volume absorption coefficient and A_{PSD} is the projected area of the PSD. Using microphysical assumptions reported in Mitchell et al. (2010) and using a tropical anvil PSD scheme, Fig. 1 shows that Q_{abs} is approximately equal in each channel for $D_e > 27$ µm, diverging for smaller D_e due to differences in Beer's Law absorption.

If the absorption efficiencies are nearly equal then the absorption optical thicknesses in these two channels are equal to a good approximation. For example, for $\delta_{CLD,A} = \{0.105, 0.358, 0.693, 1.204\}$ the corresponding $\delta_{CLD,B} = \{0.106, 0.360, 0.700, 1.216\}$. This indicates that the 13.3 and 14.2-µm cloud emissivities will be nearly equal. Computations reveal for an effective diameter of 80 µm that when $\varepsilon_A = \{0.1, 0.3, 0.5, 0.7\}$ the corresponding $\varepsilon_B = \{0.1009, 0.3025, 0.5035, 0.7036\}$. Hence we assume that they are equal, so that no new unknowns are introduced into the two-equation system when a second CO_2-channel radiance observation is added. Now we have two equations in two unknowns: cloud temperature and 13.3-µm cloud absorption optical thickness. This assumption has with it the potential to introduce errors in the retrieved cirrus temperature. Figure 2a shows that the incurred temperature-retrieval error is usually less than 0.1 K over a broad range of all-ice cirrus conditions. The temperature errors result from Q_{abs} not being exactly the same in the two CO_2 channels, and are always less than 0.14 K.

AMTD
4, 7657–7698, 2011

For liquid water clouds, the relative change in n_r (which determines the strength of tunneling contributions) is somewhat greater than for ice (see Fig. 1 in Mitchell et al., 2010). Since n_i is greater than 0.325 in both channels, Q_{abs} without tunneling will be ~1.0 for both wavelengths. The combined effects produce a larger but still modest difference in Q_{abs} shown in Fig. 1 (dashed curves), based on a mean cloud droplet diameter of 10 µm and the same ice microphysical assumptions used above. The small range of D_e is due to the liquid water fraction being 90 %, even though D_e for the ice phase extends to 139 µm. Figure 2b is like Fig. 2a but examines the condition when the liquid water fraction is 90 %. The retrieved temperature errors are less than 0.14 K at cloud temperatures above 233 K where liquid water can actually exist. Under conditions where the percentage of MODIS pixels associated with liquid or mixed phase cloud is low (as reported in Sect. 5), the retrieved mean cloud temperature error will be less than those in Fig. 2b. Note that the temperature error decreases with decreasing liquid fraction. Thus our CO_2-based cloud temperature retrieval appears quite accurate over the temperature ranges we encountered in the MODIS data sets.

Cloud effective-temperature retrievals using the two CO_2 channels were compared with MODIS-subtrack observations of cloud vertical extent. The temperatures were converted to altitude using coincident NWP temperature profiles, and then compared directly with CALIPSO lidar returns. For 22 July we obtained effective heights in the range 11–13 km, and lidar revealed the extent of the cirrus 10–15 km. For 5 August our satellite-retrieved heights were in the range 11–14 km, and lidar reported clouds in the range 8–15 km.

With the cloud physical temperature in hand we next move on to retrieving cirrus emissivities in the split window channels at 11 and 12 µm. In these window channels a simple non-scattering approach to the radiative transfer can be used, assuming emission/transmission of above-cloud water vapor is negligible. Assuming nadir viewing and cloud-filled pixels, for each infrared channel we can write:

$$I_{OBS} = (1 - \varepsilon) I_{CLR} + \varepsilon B(T_{CLD}) \,, \tag{2}$$

AMTD
4, 7657–7698, 2011

where I_{OBS} = observed radiance, I_{CLR} = clear-sky radiance obtained using Eq. (1) for a cloud-free atmosphere, ε = cirrus emissivity and $B(T_{CLD})$ = Planck function at cirrus temperature T_{CLD} (obtained from the CO_2 channels). We solve for ε_{CLD} as the only unknown:

$$\varepsilon(11\,\mu m) = \frac{I_{11,OBS} - I_{11,CLR}}{B_{11}(T_{CLD}) - I_{11,CLR}} \quad (3)$$

with a similar expression for ε (12 µm). Corresponding cloud absorption optical thicknesses δ_λ at each wavelength are obtained using

$$\delta_\lambda = -\ln(1-\varepsilon_\lambda)\,. \quad (4)$$

It is important at this point to discuss briefly any emissivity errors that are taken up into the split-window emissivity retrievals by assuming the maximum cloud-temperature error of 0.65 K shown in Fig. 2b. Assuming a cloud layer temperature of 240 K, an ocean-surface temperature of 298 K and a cloud with "true" emissivity ε (11 µm) = {0.1, 0.3, 0.5, 0.7}, then the corresponding retrieved emissivities are {0.1008, 0.3026, 0.5039, 0.7055}, each within over 99 % of their "true" values.

2.2 Effective absorption optical thickness ratio

The parameter of interest for inferring cloud microphysical attributes is the ratio of the absorption optical thicknesses at 12 and 11 µm, defined in the non-scattering case as

$$\beta = \delta_{12}/\delta_{11}\,, \quad (5)$$

which, for the flat-slab assumption, works out to be simply the ratio Q_{12}/Q_{11} of absorption efficiencies at the two wavelengths. Absorption efficiency is strongly dependent on cloud microphysical properties, and so it is sensible that their ratio is a valuable metric of cirrus microphysics. What is retrieved from satellite radiances is not truly β but an effective β, β_{eff}, that includes scattering effects. To calculate this β_{eff} in the retrieval

AMTD
4, 7657–7698, 2011

algorithm, which is β adjusted for scattering effects, we use the method described in Parol et al. (1991) and Mitchell et al. (2010):

$$\beta_{\text{eff}} = Q_{\text{abs,eff}}(12\,\mu\text{m})/Q_{\text{abs,eff}}(11\,\mu\text{m}) \quad (6)$$

and

$$Q_{\text{abs,eff}} = Q_{\text{abs}}(1-\omega_0 g)/(1-\omega_0)\,, \quad (7)$$

where g = asymmetry parameter and ω_0 = single scattering albedo of the PSD. Note that when all radiation is scattered in the forwards direction (approached in non-scattering conditions), $g = 1$ and $Q_{\text{abs,eff}} = Q_{\text{abs}}$. In the retrieval algorithm, β_{eff} is calculated from Eq. (6) using the g parameterization given in Yang et al. (2005). The effective emissivity is related to β_{eff} as described in Inoue (1985):

$$\varepsilon_{\text{eff}}(12\,\mu\text{m}) = 1-[1-\varepsilon_{\text{eff}}(11\,\mu\text{m})]^{\beta_{\text{eff}}}\,. \quad (8)$$

The optical properties of both liquid water clouds (Mitchell, 2000) and ice clouds (Mitchell, 2002) were determined using the modified anomalous diffraction approximation or MADA. MADA yields reasonably accurate and rapid calculations suitable for large volumes of satellite data and rigorously accounts for size distribution and ice crystal shape effects. For example, MADA and Mie theory agree within 10 % for liquid water clouds while laboratory ice cloud extinction measurements were predicted by MADA with 3.0 % differences on average over the size parameter range of 2 to 22. MADA errors relative to the Finite Difference Time Domain (FDTD) method for ice PSDs regarding Q_{abs} were no greater than 15 % over a wavelength range 3–100 µm for six ice particle shapes (Mitchell et al., 2006).

In this paper we extend the β_{eff} measurements in Mitchell et al. (2010) to include higher temperatures between −35 and −20 °C. Two cloud fields observed off Costa Rica on 22 July and 5 August 2007 are evaluated that correspond to clouds studied during the Tropical Composition, Cloud and Climate Coupling (TC4) field campaign. These cloud scenes are from the MODIS instrument and cover areas of roughly 65 415

AMTD
4, 7657–7698, 2011

and 41 925 km^2, respectively, assuming 1 km^2 per infrared MODIS pixel. Color composites of the cloud scenes for 22 July and 5 August 2007 are shown in Fig. 3, where yellow indicates low water cloud, white deep convective cloud and blue cirrus cloud. Figure 4 shows the same scenes but a cloud mask has been applied, showing only the cirrus clouds. In this way the cirrus clouds were isolated and evaluated in each scene. All retrievals were over ocean and correspond to single-layer clouds. Cloud emissivities, or ε, were filtered such that ε (11 µm) ≤ 0.70 for all pixels retrieved in this study. This was done so that all levels of the semi-transparent cloud contribute to the observed radiances and the radiances depend primarily on the cloud microphysics, as described in Mitchell et al. (2010). Retrievals of β_{eff} for these two days are shown in Fig. 5 as a function of retrieved temperature T. Retrievals of β_{eff} were grouped into 13 equally spaced temperature intervals to provide mean β_{eff} values and a standard deviation (σ) in β_{eff} for each T-interval.

3 Retrieval concept

Figure 5 shows that between 200 K and 235 K, mean values of β_{eff} are essentially constant with temperature, but for $T > 235$ K, the mean β_{eff} increases and rather substantially at the higher temperatures. This same β_{eff} behavior was reported in Giraud et al. (1997) where the retrieved maximum β_{eff} values were related to cloud top temperature. For $T < 235$ K, β_{eff} was constant with T, while for $T > 235$ K, β_{eff} increased, leveling off around 253 K. Subsequent analysis (Giraud et al., 2001) using the POLDER satellite instrument found that the increase in β_{eff} with higher T was due to a change in phase from ice to liquid, although there was no way to quantify the liquid fraction (i.e. the percent liquid to total condensate).

As described in Mitchell et al. (2010), β_{eff} is only sensitive to small cloud particles having maximum dimension $D \lesssim 60$ µm, with sensitivity increasing as the concentration of such particles increase. The objective of this study is to quantify this liquid fraction by extending the retrieval algorithm of Mitchell et al. (2010) to include mixed phase clouds.

AMTD
4, 7657–7698, 2011

This is only possible due to this curious relationship that Mother Nature has provided (i.e. a "flat" T-dependence of β_{eff} for glaciated conditions). Given that both glaciated and mixed phase conditions are present in a cloud field, relating β_{eff} to T should reveal a "hockey-stick" signature where the deviation from constant β_{eff} should indicate that some level of liquid water is present. The algorithm described next seeks to quantify this level.

4 Algorithm description

The retrieval algorithm used here is similar to that used in Mitchell et al. (2010), assuming a bimodal size distribution. But in the previous study, the small mode of the size distribution was comprised of ice crystals, whereas here it is assumed to be completely liquid. Consequently, the refractive indexes applied to the small mode (for calculating optical properties) correspond to liquid water. The large mode ice particle shapes are the same as in the previous study, based on TC4 measurements.

Also similar to Mitchell et al. (2010), this algorithm deals with the average behavior of the microphysics in a cloud scene, and does not address the microphysical properties of a cloud region corresponding to a single MODIS pixel. That is, the retrievals correspond to mean β_{eff} values and their standard deviations (σ) for each T-interval.

A diagram describing the principle by which the retrieval operates is described in Fig. 6. For tropical anvil clouds, a temperature dependent ice particle size distribution (PSD) scheme based on anvil clouds sampled during the Central Equatorial Pacific Experiment (CEPEX) is used to represent the ice phase (Ivanova, 2004). This PSD constituting the large particle mode is a gamma function of the form:

$$N(D) = N_0 D^{\nu} \exp(-\lambda D)\,, \tag{9}$$

where λ is the slope parameter, ν is the dispersion or width parameter, and N_0 relates the other two parameters to the PSD number concentration or IWC. A fixed IWC of

AMTD
4, 7657–7698, 2011

$10\,\mathrm{mg\,m^{-3}}$ is assumed in the algorithm (this is arbitrary and does not affect the retrieval). Retrieved cloud temperature specifies λ and $\nu = 0$ based on the CEPEX PSD measurements. The small mode of this mixed phase PSD (i.e. the cloud droplet size distribution) is also a gamma function having $\nu = 9$ which is common for liquid water clouds (Mitchell, 2000). The slope λ is determined from an assumed droplet size distribution mean diameter $\bar{d}$:

$$\lambda = (\nu + 1)/\bar{d}\,. \tag{10}$$

As discussed later, $\bar{d}$ was inferred to be between 9 and 11 µm. As described in Mitchell et al. (2010), the value of β_{eff} is calculated by initially assigning negligible liquid water content (LWC) to the small mode and calculating β_{eff} from the bimodal PSD. This is compared with the retrieved value of β_{eff}. In mixed phase conditions, the observed β_{eff} will be larger than predicted, and the LWC of the small mode is increased incrementally until the predicted and observed β_{eff} match. This yields the ratio LWC/(IWC + LWC) which is the retrieved liquid water fraction. Since we are dealing with ratios it does not matter what was initially assumed for the IWC.

The details of how this works are now described. As noted, this retrieval only considers the mean values of β_{eff} and their standard deviations when processing a cloud scene, shown by the pink curves and bars in Fig. 5. Table 1 gives the mean values of β_{eff} for the two case studies based only on the all-ice clouds ($-70\,^{\circ}\mathrm{C} < T < -38\,^{\circ}\mathrm{C}$). Adjacent to these means is the standard deviation (SD) for each mean. A threshold value β_{t} equal to the mean +2(SD) is established such that LWC is added to the small mode only when $\beta_{\mathrm{eff}} > \beta_{\mathrm{t}}$. Otherwise the cloud is assumed glaciated. Mean values of the liquid fraction can be misleading when evaluating the presence of liquid in a cloud scene since it tells nothing about the distribution of liquid fraction on the cloud scale. For this reason it is important to evaluate the liquid fraction for the positive standard deviations of β_{eff}. Table 1 also gives mean values of $(\beta_{\mathrm{eff}} + \sigma)$ where β_{eff} and σ refer to one of the means and corresponding σ shown in Fig. 5 (i.e. tops of the pink bars). To the right of this in Table 1 is the corresponding SD of mean $(\beta_{\mathrm{eff}} + \sigma)$. In retrieving the liquid fraction

AMTD
4, 7657–7698, 2011

for the standard deviations in β_{eff}, the same methodology is applied, where a threshold value β_{t} equal to the mean $(\beta_{\text{eff}} + \sigma) + 2(\text{SD})$ is established such that LWC is added to the small mode only when $\beta_{\text{eff}} > \beta_{\text{t}}$. As evident from Fig. 5, this methodology works best when a large portion of the cloud field corresponds to $T < -40\,^{\circ}\text{C}$, insuring a good baseline from which to estimate β_{t} values.

Figure 7 demonstrates the dependence of the retrieved liquid water fraction on β_{eff} and the sensitivity of the retrieval on the assumed mean cloud droplet size. It is clear that for liquid fractions more than 50 %, this retrieval will not yield accurate estimates of percent liquid water since small changes in β_{eff} result in large changes in liquid fraction. But for liquid fractions <50 %, the retrieval may yield meaningful estimates of the liquid fraction. The retrieval is shown to be sensitive to the assumed cloud droplet diameter, with the lower red curve in Fig. 7 corresponding to 9 µm and the upper curve corresponding to 11 µm. Changing the droplet dispersion parameter from 5 to 15 changed the liquid fraction by ±26 %. The retrieval is less sensitive to large particle PSD parameters since the wavelengths employed are only sensitive to particles less than ∼60 µm. For ice crystals this sensitivity is due to the photon tunneling phenomena and for water droplets this is due to Beer's Law absorption effects between wavelengths (Mitchell et al., 2010).

5 Retrieval results and uncertainties

Retrievals of the liquid fraction for the two cloud scenes are shown in Fig. 8, with the mean liquid fraction based on the mean β_{eff} over a given temperature interval, and the standard deviation corresponding to the mean liquid fraction based on the σ corresponding to the mean β_{eff}. The $\bar{d}$ assumed was 10 µm and $\nu = 9$. Although the mean liquid fractions are low, this technique is very sensitive to low levels of liquid water, as shown in Fig. 7. Liquid fraction standard deviations in Fig. 8 increase with increasing temperature for $T > -40\,^{\circ}\text{C}$. This may be due to clouds tending to be mostly liquid or mostly ice, but generally not consisting of comparable portions of both liquid

AMTD
4, 7657–7698, 2011

and ice (Korolev et al., 2003). Careful inspection of Fig. 5 at the highest temperatures reveal more points associated with the standard deviations than the means (translating to a more polarized phase partitioning), consistent with the observations in (Korolev et al., 2003). Liquid fractions greater than 50 % are not reliable, as shown by Fig. 7. Liquid fraction standard deviation values corresponding to ~60 % and 90 % in Fig. 8 may both indicate cloud conditions that are almost all liquid.

When $\bar{d}$ in the algorithm is changed to 12 µm or larger values, for all practical purposes (given the uncertainty) the algorithm predicts 100 % liquid water at temperatures corresponding to −22 and −26 °C when β_{eff} equals mean $\beta_{\text{eff}} + \sigma$ for the 5 August cloud scene. However, the value of (mean $\beta_{\text{eff}} + \sigma$) at −26 °C is clearly less than that at −22 °C. Thus the algorithm exhibits non-physical behavior for this cloud scene when $\bar{d} \geq 12$ µm. While not definitive, this information allows us to estimate that $\bar{d}$ lies between 9 and 11 µm for the 5 August cloud scene, and we assume that the same is true for the 22 July cloud scene. This is why we evaluate the algorithm sensitivity to droplet mean size in Fig. 7 using mean diameters of 9, 10 and 11 µm.

An uncertainty analysis based on varying $\bar{d}$ from 9 to 11 µm and ν from 5 to 15 is shown in Fig. 9, yielding lower and upper limit estimates for the mean β_{eff} and the mean $\beta_{\text{eff}} + \sigma$ values. The range of the uncertainty of the liquid fraction increases as the retrieved liquid fraction (mean or standard deviation) increases.

5.1 Liquid water or ice?

The aircraft cloud microphysical data from TC4 was inspected for the presence of liquid water at temperatures less than −20 °C, and no evidence of liquid was found (Lawson, 2010). However, neither the TC4 flight plans nor the microphysics data processing algorithm were designed to look for the presence of liquid water (Lawson, 2010). Conversely, recent ground-based and satellite remote sensing studies have detected liquid water between −20 and −36 °C in tropical cloud fields (Ansmann et al., 2009; Yoshida et al., 2010; Hu et al., 2010), and in situ measurements in strong updrafts of deep convective clouds have shown sustained liquid water down to −37.5 °C (Rosenfeld and

AMTD
4, 7657–7698, 2011

Woodley, 2000). Liquid water at these temperatures was almost always detected at the tops of tropical altocumulus during the Saharan Mineral Dust Experiment (Ansmann et al., 2009). These apparently conflicting results might be reconciled if a small fraction of the cloud field between −20 and −30 °C is containing significant liquid water, as the results in Fig. 5 appear to suggest. That is, the odds of a research aircraft sampling liquid water are not good if the spatial coverage and temporal frequency of liquid water is low. Moreover, the data processing algorithm used for TC4 PSD measurements selected only those periods when the mean particle size and extinction coefficient were relatively stable. Since cloud patches containing liquid would produce relatively unstable microphysical conditions, sampling intervals containing liquid may have been eliminated by the algorithm.

A retrieval methodology similar to this one has been used to estimate the PSD of ice clouds (Mitchell et al., 2010). Naturally the question may be asked "what assurance does one have that β_{eff} at warmer temperatures is not primarily due to small ice crystals?" While it is conceivable that the increase in β_{eff} is due to small ice crystals, we argue that this is very unlikely by applying the retrieval methodology of Mitchell et al. (2010) to the 5 August 2007 case study shown in Fig. 5b. The same assumptions used previously are used here, with ice crystal projected area- and mass-dimension power law relationships based on TC4 data. The anvil cirrus PSD scheme described previously is used here. The mean β_{eff} values in Fig. 5b are used in this retrieval that assumes ice-only conditions. A feature of this retrieval is the partitioning of the ice particle number concentration N into two modes; a small mode corresponding to $D < 60$ μm and a larger particle mode. The concentration ratio of the small ice crystal mode to the larger particle mode is plotted as a function of cloud temperature in Fig. 10. Ratios $\ll 1$ indicate monomodal PSD, with bimodality becoming clearly apparent for ratios $\gtrsim 1$. Strong bimodality is manifested for ratios > 10. The onset of "strong bimodality" as defined here for pure ice clouds is characterized by the peak concentration of the small mode being 10^2 higher than the peak concentration of the large mode. Figure 10 shows that predicted PSD at temperatures greater than −30 °C are strongly bimodal,

AMTD
4, 7657–7698, 2011

with N ratios reaching 250 at −20 °C. Based on the in situ PSD measurements during TC4 (Jensen et al., 2009; Lawson et al., 2010), such extreme bimodality appears unrealistic.

In Fig. 5b, note that at the warmest temperatures, the β_{eff} values are not centered on the mean but rather are clustered on either side of the mean, with many points near the standard deviations. If one applies the Mitchell et al. (2010) retrieval to estimate PSD based on the positive standard deviations of β_{eff} for $-27\,^{\circ}\text{C} < T < -20\,^{\circ}\text{C}$, N ratios range from ∼360 to 4800, and N ranges from 1.5 to 6.0 cm^{-3} for an assumed typical IWC of 10 mg m^{-3}. Such ratios appear unrealistic, and such concentrations may also be unrealistic under most conditions (Jensen et al., 2009; Zhao et al., 2011).

The PSD sampled during TC4 in relatively "fresh" anvil cirrus (attached to convective columns) are shown in Fig. 11 (see Mitchell et al., 2011a, for details). It is seen that the PSD change from monomodal to bimodal with increasing temperature, changing near $T = -40\,^{\circ}\text{C}$. A similar shift in modality occurred for aged anvil cirrus but not for in situ cirrus during TC4. Thus it is possible that the change at −40 °C in Fig. 10, from monomodal to bimodal, is initially due to ice-only PSD (note that homogeneous freezing nucleation begins ∼ −40 °C, possibly explaining the change in PSD behavior with higher nucleation rates commencing near −40 °C). However, at much warmer temperatures the bimodality in Fig. 10 appears too extreme to attribute it to the ice phase only (for reasons described above), and the observed bimodality in Fig. 11 is not that extreme.

Lastly, a split-window remote sensing study (Cooper and Garrett, 2010) found that the fraction of tropical thin cirrus comprised of small ice crystals increased from −40 to −30 °C. However, this may be a consequence of low levels of liquid water. Moreover, the 11 and 12 µm split-window method is only sensitive to particles having $D \lesssim 60$ µm and thus the actual PSD may contain significant concentrations of much larger ice particles, with the actual D_e considerably larger than the retrieved D_e if the PSD are bimodal (Mitchell et al., 2010; Mitchell and d'Entremont, 2008). That is, the retrieval may provide a D_e corresponding to a prominent small crystal mode.

AMTD
4, 7657–7698, 2011

5.2 Sensitivity to ice crystal shape

As noted, we have assumed an ice particle mass-dimension relationship based on 2D-S measurements taken during the TC4 campaign. The IWCs predicted by this relationship agree well with those measured directly by the Counterflow Virtual Impactor (CVI) instrument during TC4. To test the retrieval's sensitivity to ice particle shape, we changed this mass-dimension power law so that the ice particle mass for any given size was 50 % higher and 50 % lower than normally predicted. This resulted in a 43 % decrease and a 70 % increase in the retrieved liquid fraction at −22 °C, respectively.

Given the uncertainties in $\bar{d}$, ν and crystal shape, one could combine plausible values of these properties such that the observed increase in β_{eff} at warmer temperatures in Fig. 5 could be explained by all-ice conditions. However, the values chosen would not be supported by our best estimates of these properties, nor would the retrieved ice-only β_{eff} values be consistent with the β_{eff} derived from the PSD in situ measurements described below.

5.3 Comparison of retrieved and measurement-derived β_{eff}

Using all the TC4 PSD for anvil cirrus described in Jensen et al. (2009) and Lawson et al. (2010), β_{eff} was calculated directly from these measurements of PSD concentration, area and mass (Mitchell et al., 2011b) using both MADA and the ice crystal optical properties of Yang et al. (2005), as shown in Fig. 12. The Yang et al. optical properties were calculated using the measured PSD concentration, area and mass as described in Mitchell et al. (2011b). For all-ice clouds, β_{eff} is primarily the result of tunneling contributions that depend on particle size and shape (Mitchell et al., 2010). For a given PSD, the β_{eff} differences in Fig. 12 reflect differences in tunneling contributions. For the Yang et al. optical properties, tunneling is greatest for quasi-spherical ice particles (droxtals) and less for bullet rosettes, while the MADA treatment assumes tunneling efficiencies of 0.9 and 0.4 for the small and large particle modes of the PSD. For $T < -40$ °C, only ice exists and a direct comparison can be made between retrieved

AMTD
4, 7657–7698, 2011

and PSD-derived β_{eff} values. It is seen that the mean satellite β_{eff} value corresponds to quasi-spherical particles. This is consistent with the measured properties of TC4 cold anvil cirrus particles (Mitchell et al., 2010, 2011b). For $T > -40\,^{\circ}\text{C}$, β_{eff} for droxtals is between 1.042 and 1.022, slightly lower than our retrieved ice-only β_{eff} value of ∼1.05. This is possibly due to the deeper clouds sampled by aircraft having broader PSD relative to the thin cirrus retrieved. The main point here is that these measurement-derived β_{eff} values do not support the postulate that the increase in β_{eff} in Fig. 5 for $T > -40\,^{\circ}\text{C}$ is due to changes in ice crystal habit.

5.4 Vertical phase partitioning

Having the upper cloud layer composed mostly of liquid water, with the bottom layer mostly ice (e.g. Ansmann et al., 2009), or vice-versa, should not affect this retrieval significantly since only cloudy pixels with ε (11 µm) ≤ 0.70 were analyzed. Thus all cloud levels contribute significantly to the radiance observed by the satellite sensor, yielding an integrated assessment of liquid fraction through the cloud layer.

5.5 CALIPSO retrievals

The MODIS scenes used here are from the AQUA satellite, part of the A-train constellation of satellites. The CALIPSO satellite is also part of the A-train, and the CALIPSO lidar (CALIOP) is used to discriminate the thermodynamic phase of the underlying clouds, based on the algorithm of Hu et al. (2009). Phase discrimination is based primarily on lidar depolarization ratios since backscattered light from ice crystals is depolarizing while backscattered light from liquid water droplets has minimal depolarization. However, horizontally oriented ice particles exhibit relatively weak depolarization, similar to liquid water clouds. The Hu et al. (2009) algorithm applies a spatial coherence analysis technique to separate water clouds from ice clouds dominated by horizontally oriented particles. It thus discriminates well between liquid and ice clouds and also

AMTD
4, 7657–7698, 2011

separates ice clouds into two categories, with and without a dominance of horizontally oriented ice particles.

The two CALIPSO/CALIOP cloud phase discrimination analyses coincident with the two MODIS scenes evaluated in this study are shown in Fig. 13, residing within the dashed boxes. Due to the narrow field-of-view of the CALIOP lidar, only a narrow path of clouds was sampled compared to the MODIS scenes. Nonetheless, the lidar analysis reveals the presence of liquid-dominated cloud under the CALIOP flight path corresponding to the two MODIS scenes, mostly between 7 and 9.5 km. There is also a considerable amount of cloud classified as "unknown", which could be either liquid water or ice dominated. Thus the CALIOP phase analysis appears consistent with our column integrated analysis for single-layer high clouds at various altitudes over ocean.

6 Cloud optical property dependence on liquid fraction

In addition to the liquid fraction, this algorithm also predicts the vertically integrated cloud effective diameter D_e that depends on both the liquid and ice phases. The effective diameter is defined here as

$$D_e = (3/2)\mathrm{TWC}/[(f_i\rho_i + f_w\rho_w)P_t], \quad (11)$$

where TWC is the total water content, ρ_i is the density of bulk ice ($0.917\,\mathrm{g\,cm^{-3}}$), ρ_w is the density of bulk water ($1.0\,\mathrm{g\,cm^{-3}}$), f_i and f_w are the ice and liquid water fractions (relative to TWC), and P_t is the total projected area of the size distribution (including water and ice). This definition is universal for both water and ice clouds (Mitchell, 2002).

Shown in Fig. 14 is the D_e dependence on temperature for the cloud scene of 5 August 2007. The blue curve gives D_e based on mean β_{eff} values while the pink curve gives D_e based on mean $\beta_{eff} + \sigma$ values. Since D_e is a measure of the cloud optical properties, this illustrates how D_e and hence optical properties are affected by

AMTD
4, 7657–7698, 2011

low levels of liquid water in cloud fields that are primarily ice. Since the extinction coefficient at solar wavelengths can be expressed as

$$\beta_{\text{ext}} \approx 3\text{TWC}/(\rho D_{\text{e}}) , \quad (12)$$

where ρ is the weighted density shown in Eq. (11), it is evident that an increase in the mean liquid fraction from 0 to 12 % results in a change in mean D_{e} from ∼113 µm (pure ice cloud) to 73 µm, or an increase in extinction of ∼ 55 % for constant TWC. Moreover, 16 % of the clouds experience a change in D_{e} from ∼86 to ∼20 µm, which is over a three-fold increase in β_{ext}. It is therefore apparent that low levels of liquid water in clouds primarily containing ice need to be accounted for to accurately describe their radiative properties and the global radiation budget in general.

The cause of these low levels of liquid water between −38 and −20 °C is not clear, but high levels of sustained liquid water have been measured in deep tropical convection (Rosenfeld and Woodley, 2000), and liquid appears to dominate during the early development of tropical altocumulus and remains at the tops of such clouds in this temperature range (Ansmann et al., 2009). It is possible that gravity waves due to deep convection may be producing transient regions of liquid water. Clearly more research is needed in understanding the causes for liquid water in tropical clouds between −38 and −20 °C. If indeed appreciable liquid water does exist in tropical cloud fields at these temperatures, such clouds will be susceptible to the first indirect aerosol effect since the liquid phase could dominate their optical properties.

7 Summary and concluding remarks

A new satellite remote sensing method has been described for retrieving the cloud temperature and emissivities in two split-window channels (11 and 12 µm). This differed from other studies in that all three of these properties were retrieved independently without estimating temperature from a nearby optically thick cloud evaluated as a "black body" emitter. This allowed the effective 12-to-11 µm cloud absorption optical

AMTD
4, 7657–7698, 2011

thickness ratio, or β_{eff}, to be related to retrieved cloud temperature, revealing how cloud microphysical characteristics change with temperature. The satellite observations from this and another study (Giraud et al., 1997, 2001), that show β_{eff} is approximately constant with temperature for all-ice conditions, provided a means for estimating the cloud liquid fraction as β_{eff} increases for $T > -40\,^{\circ}\text{C}$. Although uncertainties are large due to unknown parameters in the cloud droplet size distribution and ice particle shape, the retrievals do show the increasing likelihood of liquid water as temperatures increase between -40 and $-20\,^{\circ}\text{C}$. Our best estimates for two MODIS tropical cloud scenes (where a cloud mask was applied to remove all clouds that did not appear to be cirrus) suggest the liquid fraction in both cases is around 10 % on average for $T \approx -22\,^{\circ}\text{C}$. However, about 16 % of the cloud pixels at this temperature appear to be liquid water dominated, and the individual pixel retrievals of β_{eff} suggest that individual clouds tend to be either ice or liquid water dominated. To our knowledge this type of information did not previously exist regarding widespread tropical cloud fields characterized by deep convection.

In addition to these main results, this remote sensing method when assuming all-ice conditions predicts a change from mono-modal to bimodal ice size-spectra near $-40\,^{\circ}\text{C}$ (bimodal for $T > -40\,^{\circ}\text{C}$). This is what was observed from aircraft measurements of anvil cirrus (Mitchell et al., 2011a) and mid-latitude synoptic cirrus (Mitchell et al., 2011c) in the absence of liquid water, suggesting the retrieved change in modality could be partly due to the onset of homogeneous freezing nucleation. However, low levels of liquid may also be responsible for the retrieved β_{eff} values. Indeed, the bimodality predicted by the retrieval between -30 and $-20\,^{\circ}\text{C}$ appears too extreme to be attributed to the ice phase alone but is quite compatible with the presence of liquid water. Another interesting result was the consistency between the ice particle shapes observed during TC4 and those used in the retrieval to achieve consistency between retrieved and in situ measured β_{eff} values. This result reinforces findings from in situ measurements, indicating that quasi-spherical and/or compact, high density ice particles dominated thin cirrus during TC4.

AMTD
4, 7657–7698, 2011

Future work should refine this satellite retrieval by using in situ data from recent ice cloud field campaigns to better characterize cloud physical properties that pertain to the a priori retrieval assumptions (e.g. mean droplet size, ice PSD and particle shape). This same in situ data could be used to test the retrieval when possible. This satellite retrieval could be applied to other types of cold cloudy environments to better characterize mixed phase conditions, provided the mean liquid fraction is less than 50 %. Aircraft measurements in mixed phase clouds show great variability in the liquid fraction from study to study (Korolev et al., 2003), making it difficult to determine the average and statistical behavior of the liquid fraction with temperature. But with satellite methods this can potentially be done to some extent. This methodology could also be used to evaluate the impact of dust episodes on cloud glaciation and possibly other aspects of ice nucleation.

This methodology could be applicable to other satellite sensors with CO_2 and thermal infrared window bands such as EOS AIRS or the Cross-track Infrared Sounder (CrIS) on the NPP satellite. The NOAA/NASA GOES-R satellite system will be launched in 2015 and will contain channels at 10.35, 11.2, 12.3 and 13.3 µm having 2 km spatial resolution. It appears possible that some combination of these channels could be exploited as described here (albeit with more uncertainty in the temperature retrieval) to obtain time-dependent information on the phase composition of high clouds at a given location.

As mentioned, cloud phase information is sorely needed for testing the cloud parameterizations in climate models. For example, GCMs differ considerably in their albedo predictions from frontal cloud systems, and much of these differences were due to the treatment of cloud phase partitioning (Hu et al., 2010). One reason information about the liquid fraction is so crucial in high clouds is its large impact on the cloud optical properties, with a 10 % liquid fraction increasing cloud optical thickness by more than 50 % relative to all-ice conditions.

AMTD
4, 7657–7698, 2011

Acknowledgements. This research was primarily sponsored by the Office of Science (BER), US Dept. of Energy, Grant DE-FG02-06 ER64201. We also gratefully acknowledge the contributions of John Eylander at the US Air Force Weather Agency for supporting the development of the satellite-based emissivity retrievals. Additional support from NASA EPSCoR under Cooperative Agreement No. NNX10AR89A is gratefully acknowledged. We are grateful to Paul Lawson for providing the TC4 in situ data. This work began as a ground-based mixed-phase cloud retrieval study, but as research evolved it was apparent that the methodology was best suited for satellite remote sensing.

References

Ansmann, A., Tesche, M., Seifert, P., Althausen, D., Engelmann, R., Fruntke, J., Wandinger, U., Mattis, I., and Müller, D.: Evolution of the ice phase in tropical altocumulus: SAMUM lidar observations over Cape Verde, J. Geophys. Res., 114, D17208, doi:10.1029/2008JD011659, 2009.

Cooper, S. and Garrett, T.: Identification of small ice cloud particles using passive radiometric observations, J. Appl. Meteorol. Clim., 49, 2334–2347, 2010.

Curry, J. A., Rossow, W. B., Randall, D., and Schramm, J. L.: Overview of Arctic cloud and radiation characteristics, J. Climate, 9, 1731–1764, 1996.

Fleishauer, V., Larson, V. E., and Vonder Haar, T. H.: Observed microphysical structure of midlevel, mixed-phase clouds, J. Atmos. Sci., 59, 1779–1804, 2002.

Giraud, V., Buriez, J. C., Fouquart, Y., and Parol, F.: Large-scale analysis of cirrus clouds from AVHRR data: assessment of both a microphysical index and the cloud-top temperature, J. Appl. Meteorol., 36, 664–674, 1997.

Giraud, V., Thouron, O., Reidi, J., and Goloub, P.: Analysis of direct comparison of cloud top temperature and infrared split window signature against independent retrievals of cloud thermodynamic phase, Geophys. Res. Lett., 28, 983–986, 2001.

Heymsfield, A. J., Milosevich, L. M., Slingo, A., Sassen, K., and Starr, D. O. C.: An observational and theoretical study of highly supercooled altocumulus, J. Atmos. Sci., 48, 923–945, 1991.

Hobbs, P. V. and Rangno, A. L.: Ice particle concentrations in clouds, J. Atmos. Sci., 42, 2523–2549, 1985.

AMTD

4, 7657–7698, 2011

Hobbs, P. V. and Rangno, A. L.: Microstructures of low and middle-level clouds over the Beaufort Sea, Q. J. Roy. Meteorol. Soc., 124, 2035–2071, 1998.
Inoue, T.: On the temperature and emissivity determination of semitransparent cirrus clouds by bispectral measurements in the 10 μm window region, J. Meteorol. Soc. Jpn., 63, 88–98, 1985.
Ivanova, D.: Cirrus clouds parameterization for global climate models (GCMs) and North American (Mexican) monsoon modeling study, Ph.D. dissertation, University of Nevada, Reno, 181 pp., 2004.
Jensen, E. J., Lawson, P., Baker, B., Pilson, B., Mo, Q., Heymsfield, A. J., Bansemer, A., Bui, T. P., McGill, M., Hlavka, D., Heymsfield, G., Platnick, S., Arnold, G. T., and Tanelli, S.: On the importance of small ice crystals in tropical anvil cirrus, Atmos. Chem. Phys., 9, 5519–5537, doi:10.5194/acp-9-5519-2009, 2009.
Korolev, A. V., Isaac, G. A., Cober, S. G., Strapp, J. W., and Hallett, J.: Microphysical characterization of mixed phase clouds, J. R. Meteorol. Soc., 129, 39–65, 2003.
Lawson, R. P., Baker, B. A., Schmitt, C. G., and Jensen, T. L.: An overview of microphysical properties of Arctic clouds observed in May and July 1998 during FIRE ACE, J. Geophys. Res., 106, 14989–15014, 2001.
Lawson, R. P., Jensen, E., Mitchell, D. L., Baker, B., Mo, Q., and Pilson, B.: Microphysical and radiative properties of tropical clouds investigated in TC4 and NAMMA, J. Geophys. Res., 115, D00J08, doi:10.1029/2009JD013017, 2010.
Li, Z.- X. and Le Treut, H.: Cloud-radiation feedbacks in a general circulation model and their dependence on cloud modeling assumptions, Clim. Dynam., 7, 133–139, 1992.
Matveev, L. T.: Cloud Dynamics, Atmospheric and Oceanic Sciences Library Series, vol. 2, D. Reidel, 340 pp., 1984.
Mitchell, D. L.: Parameterization of the Mie extinction and absorption coefficients for water clouds, J. Atmos. Sci., 57, 1311–1326, 2000.
Mitchell, D. L.: Effective diameter in radiation transfer: general definition, applications and limitations, J. Atmos. Sci., 59, 2330–2346, 2002.
Mitchell, D. L. and d'Entremont, R. P.: Satellite remote sensing of small ice crystal concentrations in cirrus clouds, in: Proc. 15th Int. Conf. on Clouds and Precipitation, Cancun, Mexico, ICCP, 185–188, 2008.
Mitchell, D. L., Baran, A. J., Arnott, W. P., and Schmitt, C.: Testing and comparing the modified anomalous diffraction approximation, J. Atmos. Sci., 63, 2948–2962, 2006.

AMTD
4, 7657–7698, 2011

Mitchell, D. L., d'Entremont, R. P., and Lawson, R. P.: Inferring cirrus size distributions through satellite remote sensing and microphysical databases, J. Atmos. Sci., 67, 1106–1125, 2010.
Mitchell, D. L., Mishra, S., and Lawson, R. P.: Representing the ice fall speed in climate models: Results from TC4 and ISDAC, J. Geophys. Res., 116, D00T03, doi:10.1029/2010JD015433, 2011a.
Mitchell, D. L., Lawson, R. P., and Baker, B.: Understanding effective diameter and its application to terrestrial radiation in ice clouds, Atmos. Chem. Phys., 11, 3417–3429, doi:10.5194/acp-11-3417-2011, 2011b.
Mitchell, D. L., Mishra, S., and Lawson, R. P.: Cirrus Clouds and Climate Engineering: New Findings on Ice Nucleation and Theoretical Basis, Planet Earth 2011 - Global Warming Challenges and Opportunities for Policy and Practice, edited by: Carayannis, E. G., available at: http://www.intechopen.com/articles/show/title/cirrus-clouds-and-climate-engineering-new-findings-on-ice-nucleation-and-theoretical-basis, last access: 16 December 2011, InTech, ISBN 978-953-307-733-8, 2011c.
Moncet, J.-L, Uymin, G., Lipton, A. E., and Snell, H. E.: Infrared radiance modeling by optimal spectral sampling, J. Atmos. Sci., 65, 3917–3934, 2004.
Nalli, N. R., Minnett, P. J., and van Delst, P.: Emissivity and reflection model for calculating unpolarized isotropic water surface-leaving radiance in the infrared, I: Theoretical development and calculations, Appl. Optics, 47, 3701–3721, 2008.
Parol, F., Buriez, J. C., Brogniez, G., and Fouquart, Y.: Information content of AVHRR channels 4 and 5 with respect to the effective radius of cirrus cloud particles, J. Appl. Meteorol., 30, 973–984, 1991.
Pinto, J. O., Curry, J. A., and Intrieri, J. M.: Cloud-aerosol interactions during autumn over Beaufort Sea, J. Geophys. Res., 106, 15077–15097, 2001.
Rosenfeld, D. and Woodley, W.: Deep convective clouds with sustained supercooled liquid water down to −37.5 °C, Nature, 405, 440–442, 2000.
Shupe, M. D. and Intrieri, J. M.: Cloud radiative forcing of the Arctic surface: the influence of cloud properties, surface albedo and solar zenith angle, J. Climate, 17, 616–628, 2004.
Shupe, M. D., Kollias, P., Matrosov, S. Y., and Schneider, T. L.: Deriving mixed-phase cloud properties from Doppler radar spectra, J. Atmos. Ocean. Tech., 21, 660–670, 2004.
Turner, D. D.: Arctic mixed-phase cloud properties from AERI lidar observations: algorithm and results from SHEBA, J. Appl. Meteorol., 44, 427–444, 2005.

AMTD
4, 7657–7698, 2011

Warren, S. G., Hahn, C. J., London, J., Chervin, R. M., and Jenne, R.: Global distribution of total cloud cover and cloud type amount over land, NCAR Tech. Note TN-317 STR, 212 pp., 1988.

Yang, P., Wei, H., Huang, H.-L., Baum, B. A., Hu, Y. X., Kattawar, G. W., Mishchenko, M. I., and Fu, Q.: Scattering and absorption property database for nonspherical ice particles in the near- through far-infrared spectral region, Appl. Optics, 44, 5512–5523, 2005.

Yoshida, R., Okamoto, H., Hagihara, Y., and Ishimoto, H.: Global analysis of cloud phase and ice crystal orientation from Cloud-Aerosol Lidar and Infrared Pathfinder Satellite Observation (CALIPSO) data using attenuated backscattering and depolarization ratio, J. Geophys. Res., 115, D00H32, doi:10.1029/2009JD012334, 2010.

Zhao, M. and Wang, Z.: Comparison of Arctic clouds between ECMWF simulations and ACRF long-term observations at the NSA Barrow site, J. Geophys. Res., 115, D23202, doi:10.1029/2010JD014285, 2010.

Zhao, Y., Mace, G., and Comstock, J.: The occurrence of particle size distribution bimodality in middle latitude cirrus as inferred from ground-based remote sensing data, J. Atmos. Sci., 68, 1162–1177, doi:10.1175/2010JAS3354.1, 2011.

AMTD
4, 7657–7698, 2011

Table 1. Mean values of retrieved β_{eff} and $(\beta_{\text{eff}}+\sigma)$, with corresponding values of their standard deviations (SD) for the two case studies. β_{eff} is the effective 12-to-11 µm absorption optical thickness ratio and its SD at a given temperature is given by σ.

Date	Temperature interval (°C)	Mean β_{eff}	SD	Mean $(\beta_{\text{eff}}+\sigma)$	SD
22 July 2007	–69 to –38	1.0539	0.0042	1.0891	0.0133
5 August 2007	–70 to –38	1.0474	0.0018	1.0801	0.0080

AMTD
4, 7657–7698, 2011

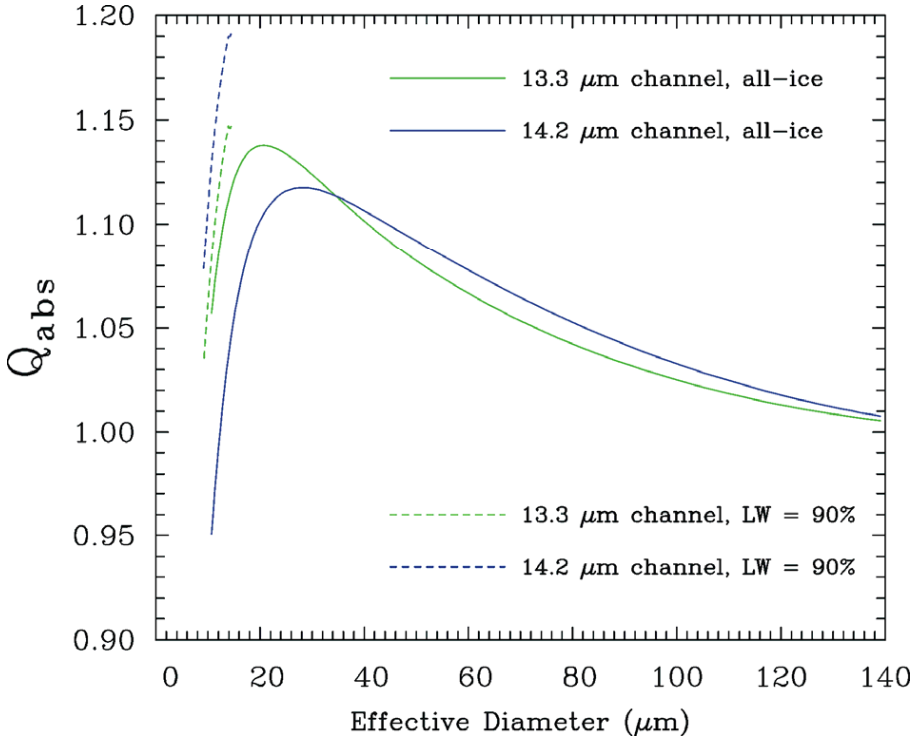

Fig. 1. Testing the temperature retrieval for all-ice and primarily liquid water (LW) conditions over a broad range of ice phase D_e. Q_{abs} is the area-weighted absorption efficiency of an ice particle size distribution (PSD), calculated here for two of the MODIS CO_2 channels. See text for details.

AMTD
4, 7657–7698, 2011

Satellite retrieval of liquid water fraction in tropical clouds

D. L. Mitchell and
R. P. d'Entremont

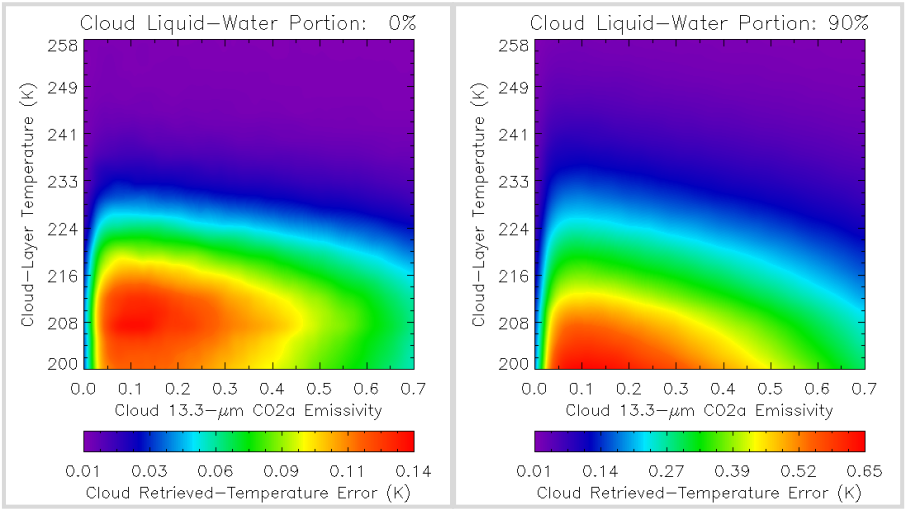

Fig. 2. Retrieved temperature error for (left panel) glaciated clouds and (right panel) mixed phase clouds having 90 % liquid water. Clouds are described by their mid-layer temperature and their emissivity at 13.3 μm, with colors showing the temperature error in the retrieval. See text for details.

AMTD
4, 7657–7698, 2011

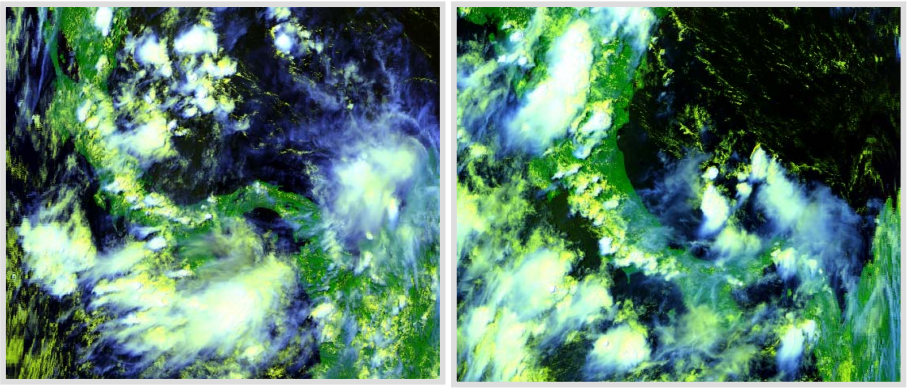

Fig. 3. Cloud scenes over Costa Rica on 22 July (left panel) and 5 August 2007 (right panel) during the NASA TC4 experiment. Blue colors indicate cirrus clouds, white is deep convection and yellow indicates liquid water clouds.

AMTD
4, 7657–7698, 2011

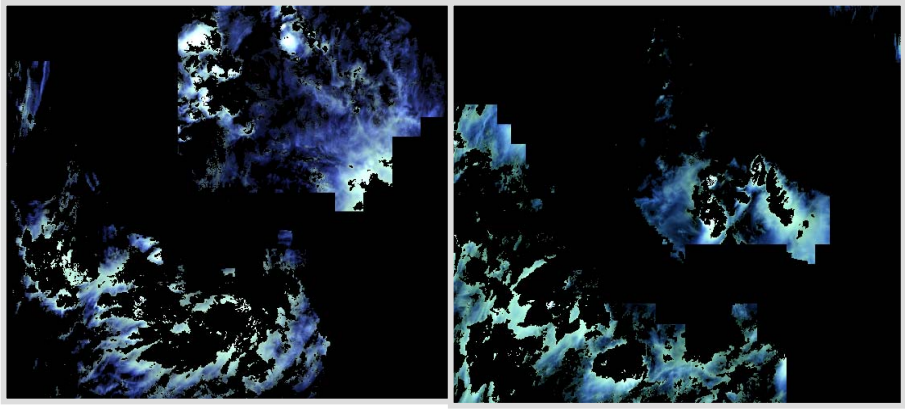

Fig. 4. Same as Fig. 3 except a cloud mask was applied to show only cirrus clouds (white-to-blue colors).

AMTD
4, 7657–7698, 2011

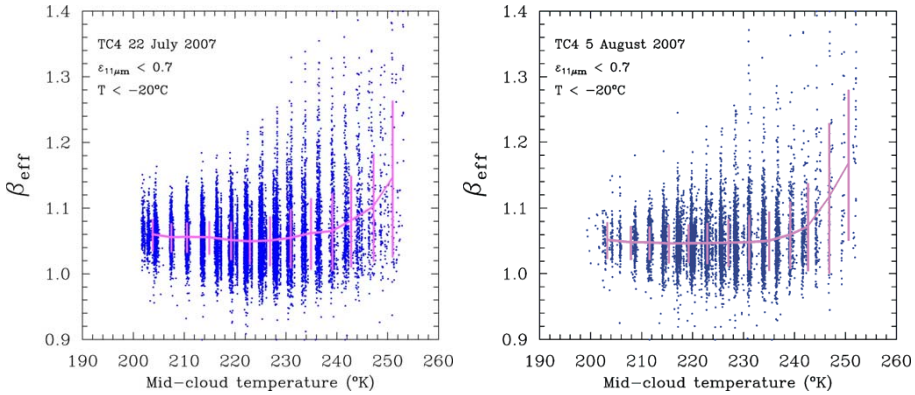

Fig. 5. Retrievals of the effective absorption optical thickness ratio related to retrieved mid-cloud temperature for **(a)** the 22 July cloud scene and **(b)** the 5 August cloud scene. Cloudy pixels were filtered so that only pixels having 11 μm emissivities less than 0.7 and temperatures less than −20 °C were used.

AMTD
4, 7657–7698, 2011

Satellite retrieval of liquid water fraction in tropical clouds

D. L. Mitchell and R. P. d'Entremont

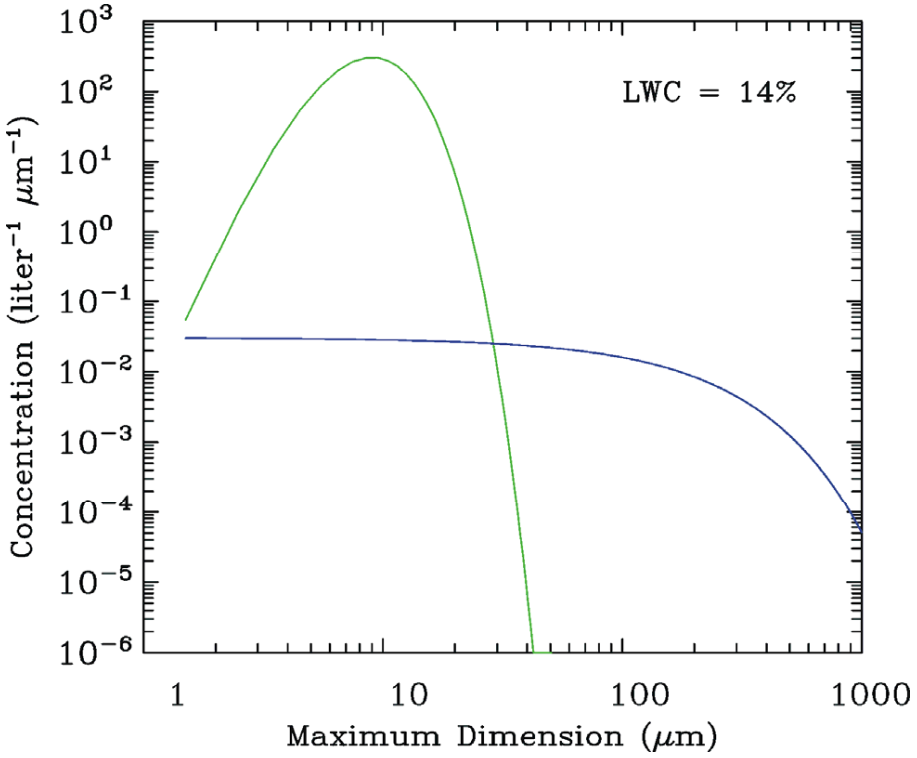

Fig. 6. Algorithm framework with a variable droplet size distribution in green and a temperature-dependent anvil cirrus PSD in blue. The liquid water content (LWC) of the droplet size distribution shown here is 14 % of the total condensate (liquid + ice).

AMTD
4, 7657–7698, 2011

Satellite retrieval of liquid water fraction in tropical clouds

D. L. Mitchell and
R. P. d'Entremont

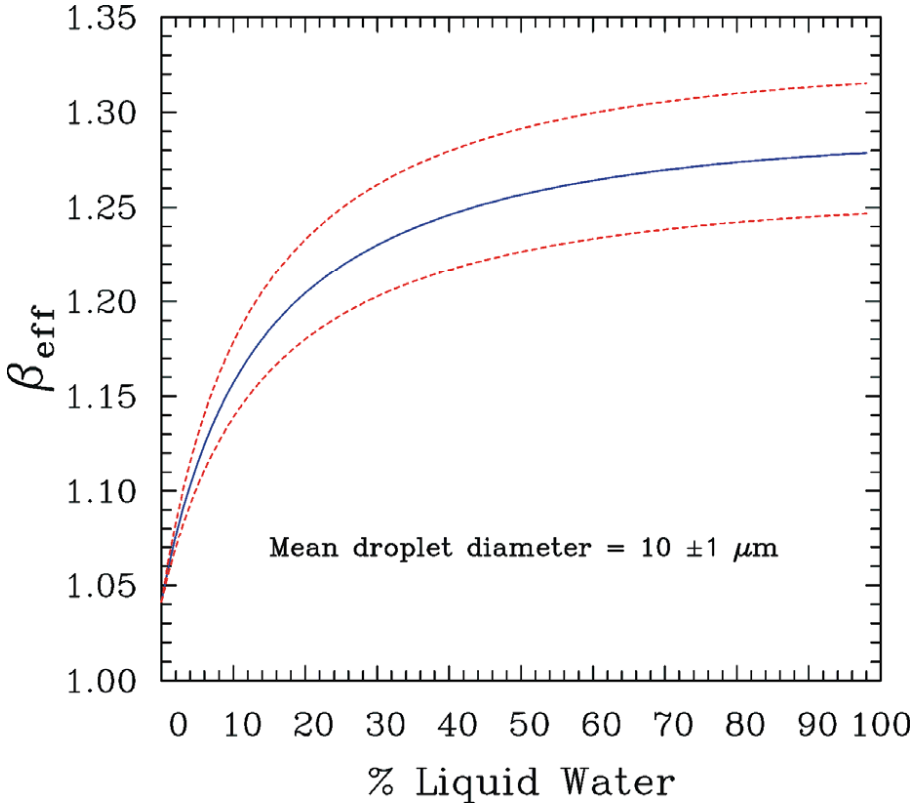

Fig. 7. Dependence of the retrieved liquid water fraction on β_{eff} and the sensitivity of the retrieval on the assumed mean cloud droplet size. The blue curve is for a mean size of 10 μm while the two red dashed curves are for mean droplet sizes of 9 (lower) and 11 (upper) μm.

AMTD
4, 7657–7698, 2011

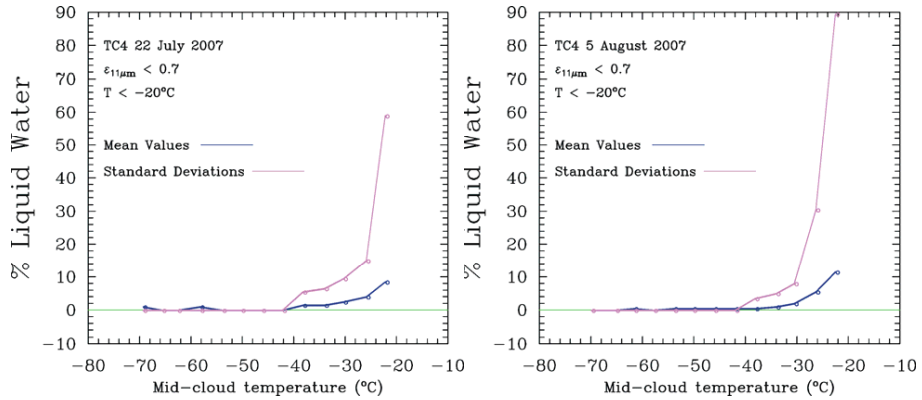

Fig. 8. Retrieved liquid fraction for clouds identified as single-layer cirrus for the two cloud scenes studied. Both means and standard deviations are plotted against retrieved temperature as described in the text. Cloud emissivities (at 11 μm) and temperatures were less than 0.7 and −20 °C, respectively.

AMTD
4, 7657–7698, 2011

Satellite retrieval of liquid water fraction in tropical clouds

D. L. Mitchell and
R. P. d'Entremont

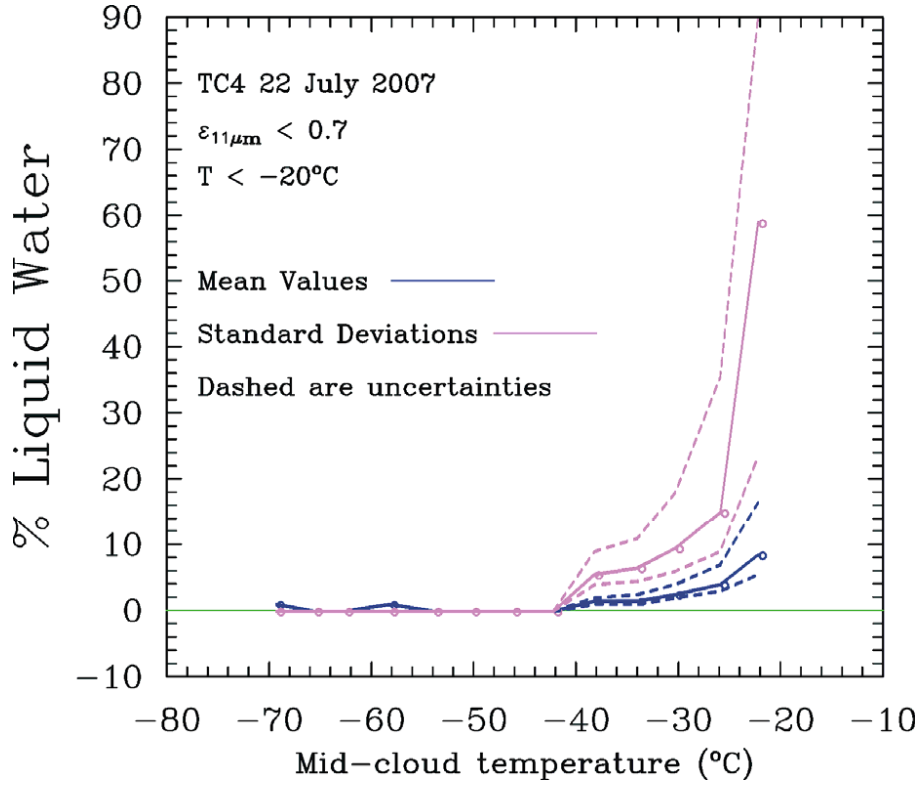

Fig. 9. Uncertainty estimates (dashed) for the means and standard deviations (solid) in Fig. 8a.

AMTD
4, 7657–7698, 2011

Satellite retrieval of liquid water fraction in tropical clouds

D. L. Mitchell and
R. P. d'Entremont

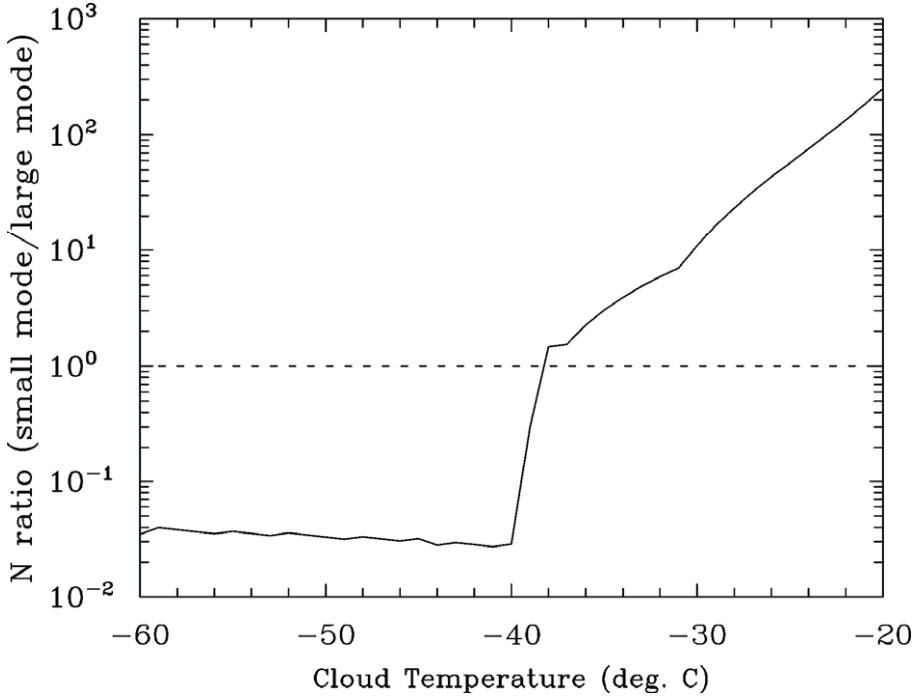

Fig. 10. Retrieval of PSD bimodality for the 5 August 2007 case study, based on the mean β_{eff} values in Fig. 5b assuming all-ice conditions. Bimodality is evaluated using the N ratio (ice particle concentration of small mode/large mode) with N ratio ~1 roughly separating unimodal from bimodal PSDs.

AMTD
4, 7657–7698, 2011

Satellite retrieval of liquid water fraction in tropical clouds

D. L. Mitchell and
R. P. d'Entremont

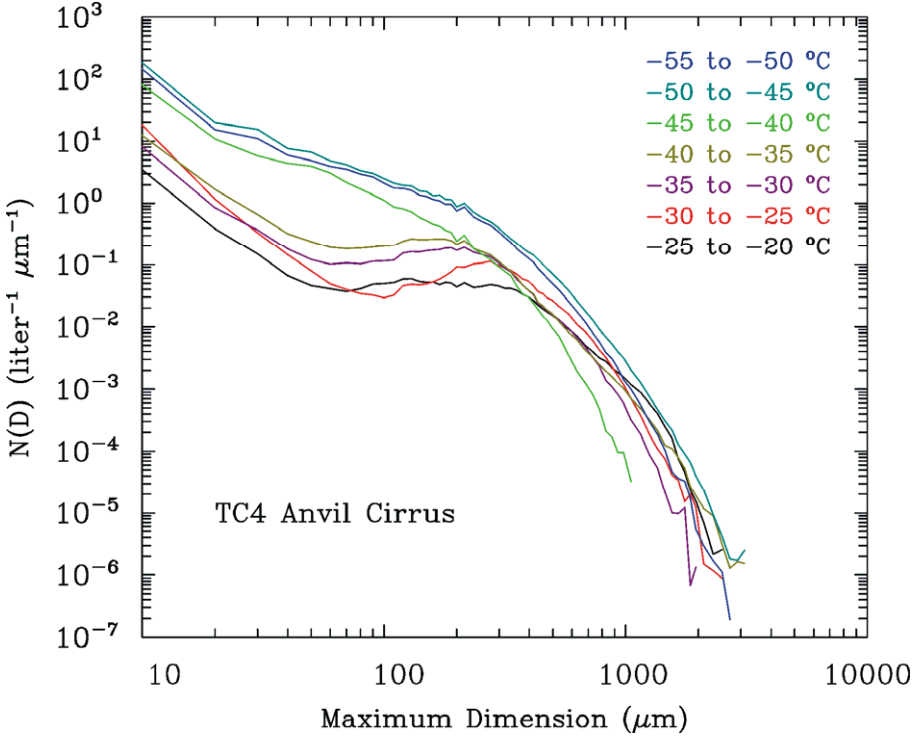

Fig. 11. Mean PSD (averaged over intervals of 5 °C) from "fresh" anvil cirrus sampled during TC4.

AMTD
4, 7657–7698, 2011

Satellite retrieval of liquid water fraction in tropical clouds

D. L. Mitchell and
R. P. d'Entremont

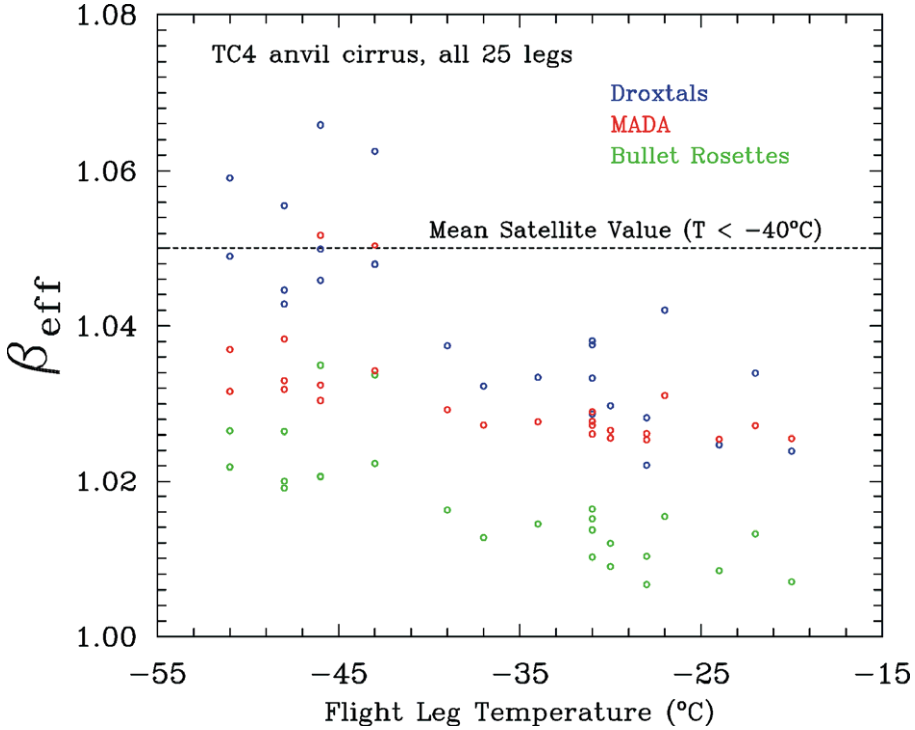

Fig. 12. Calculations of β_{eff} from TC4 in situ measurements of fresh anvil cirrus using two ice optics schemes, MADA and Yang et al., 2005 (i.e. droxtals and bullet rosettes). The satellite-retrieved mean value of β_{eff}, based on this study for $T < -40\,^{\circ}$C, is shown by the dashed line. A direct comparison between retrieved and measured β_{eff} can be made for $T < -40\,^{\circ}$C, suggesting quasi-spherical particles (i.e. droxtals) dominate, which was validated via in situ measurements.

AMTD
4, 7657–7698, 2011

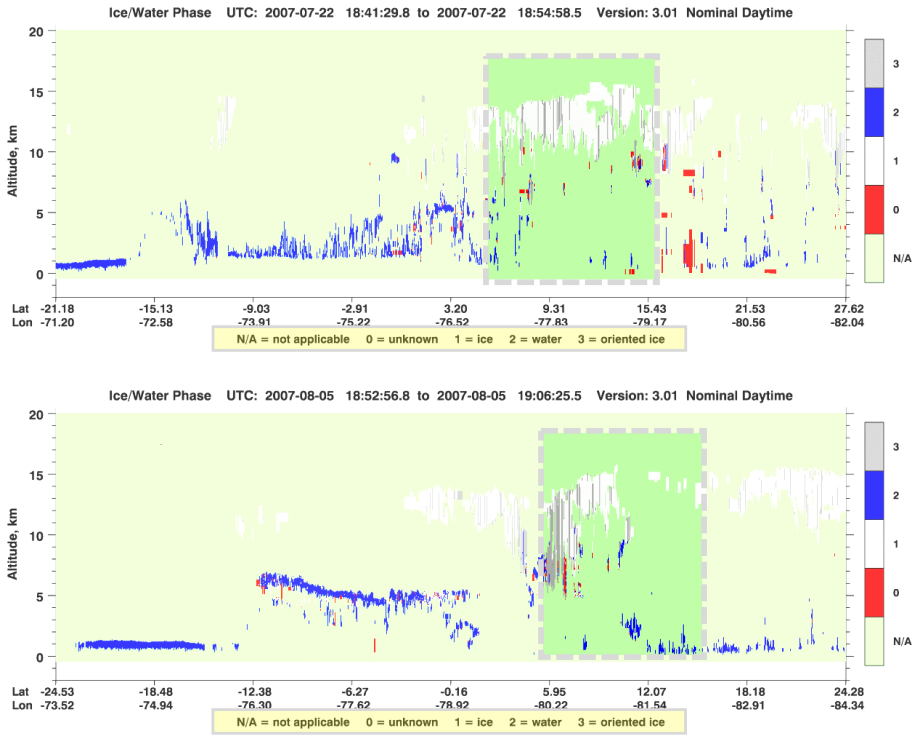

Fig. 13. CALIPSO/CALIOP discrimination of cloud phase for the two days studied here. The TC4 region considered in this study is bounded by the dashed box containing the green background. Blue and possibly red regions are dominated by liquid water. While coincident with MODIS sampling, the CALIPSO instrument samples only a narrow swath of the MODIS cloud scene due to the narrow field-of-view of the CALIOP lidar.

AMTD
4, 7657–7698, 2011

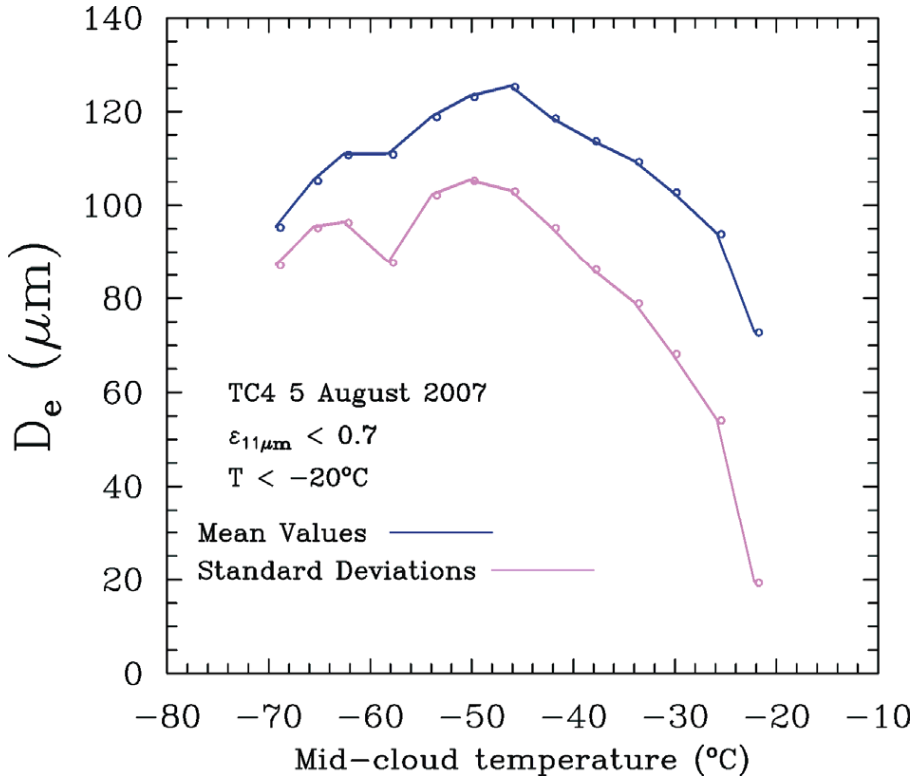

Fig. 14. Impact of the liquid fraction on the combined-phase effective diameter D_e corresponding to the means and standard deviations of β_{eff}, for the 5 August 2007 case study. The liquid fraction near −22 °C is about 12 %.

AMTD
4, 7657–7698, 2011

Satellite retrieval of liquid water fraction in tropical clouds

D. L. Mitchell and
R. P. d'Entremont